Bulletin of the Seismological Society of America, Vol. 102, No. 2, pp. 467–478, April 2012, doi: 10.1785/0120110163

Yield Estimation of the 25 May 2009 North Korean Nuclear Explosion

by Lian-Feng Zhao, Xiao-Bi Xie, Wei-Min Wang, and Zhen-Xing Yao

Abstract We collect nine vertical component broadband seismograms from the 25 May 2009 North Korean nuclear explosion for a regional seismic network in which eight stations also recorded the 9 October 2006 North Korean nuclear test. Comparing the observed waveforms and spectra from the two events, we estimate that the amplitudes of the records from the second event are approximately five times those from the first one. Additionally, we use 599 vertical broadband seismograms from 82 regional events recorded on the regional network between December 1995 and May 2009 to calibrate the network *Lg*-wave magnitude. The calibrated network is used to calculate the *Lg*-wave body-wave magnitude $m_b(Lg) = 4.53$ for the 25 May 2009 North Korean nuclear explosion. Based upon 15 first arrivals from the two North Korea nuclear explosions, the regional *Pn* velocity in the northeast China–North Korea region is calculated to be 8.0 km/s. This result, along with the regional geological structures, suggests that the North Korean test site (NKTS) is located at a relatively stable continental region. We thus use a modified fully coupled magnitude–yield relation to estimate the explosion yield, and the result shows that the yield of the 25 May 2009 North Korean nuclear test is approximately 2.35 kt under the minimum burial depth assumption.

Online Material: Epicentral parameters, computed $m_b(Lg)$, and corrected $m_b(Lg)$ for 82 events used in the study.

Introduction

North Korea conducted its second underground nuclear test (NKT2) on 25 May 2009. The United States Geological Survey (USGS) National Earthquake Information Center (NEIC) Preliminary Determination of Epicenters (PDE) reported the body-wave magnitude to be m_b 4.7 and the origin time to be 00:54:43 UTC. The epicenter was located at 41.33° N and 129.01° E, near the test site of the first North Korean nuclear test (NKT1) on October 9, 2006. Both events generated abundant regional seismic phases in northeast China and the Korean Peninsula, traversing continental crust. The regional phases *Pn*, *Pg*, *Lg*, and Rayleigh waves were clearly seen in seismograms. Due to its larger magnitude, seismic records from NKT2 have larger signal-to-noise ratios than those from NKT1. Seismic data from the two nuclear explosions provided crucial information and triggered great research interest in explosion yield estimation and discrimination between explosion and earthquake sources in the Korean peninsula (Kim and Richards, 2007; Kvaerna *et al.*, 2007; Salzberg and Marshall, 2007; Bonner *et al.*, 2008; Koper *et al.*, 2008; Hong *et al.*, 2008; Patton and Taylor, 2008; Tibuelac *et al.*, 2008; Zhao *et al.*, 2008; Hong and Rhie, 2009; Kim *et al.*, 2009; Murphy *et al.*, 2010; Ni *et al.*, 2010; Schlittenhardt *et al.*, 2010; Shin *et al.*, 2010; Rougier *et al.*, 2011).

Two regional waveforms recorded at the same instrument are likely to show great similarity when the corresponding events occur within very close proximity and were associated with similar focal mechanisms (Schaff and Richards, 2004). Waveform correlation has been used to measure very small differential travel times from event pairs recorded at a network of stations to provide highly improved relative location estimates of nuclear explosions and earthquakes (e.g., Poupinet *et al.*, 1984; Shearer, 1997; Phillips *et al.*, 2001; Shearer *et al.*, 2003; Waldhauser *et al.*, 2004). Wen and Long (2010) obtained the high-precision location of NKT2 to be 41.29° N and 129.08° E based on the *Pn* differential travel times measured by waveform cross-correlation. The cross-correlation was also used to measure the waveform coherence, including both amplitude and phase (Schimmel, 1999). Salzberg and Marshall (2007) developed a semi-empirical method, which links seismic data from different events recorded at the same station. With this method, they investigated the yield of NKT1. Using a Chinese chemical explosion with known yield as a reference, they calibrated the seismic record of NKT1 at station MDJ and estimated the yield to be approximately 0.45 kt. Their result is similar to that estimated from the regional *Lg*-wave magnitude by Zhao *et al.* (2008). By comparing the *Pn* and *Pg* spectra

from the two North Korean nuclear tests, Kim *et al.* (2009) estimated that the mean yield ratio for these events ranges between 3.45 and 6.36 over the 95% confidence interval. In this study we will analyze the regional waveform coherencies of different regional phases from the two North Korean nuclear tests.

The *Lg* wave is usually the largest phase at regional distances and can give stable and accurate magnitude estimates if a proper attenuation model is available. The regional magnitude based on *Lg*-wave has been well developed and applied (Nuttli, 1973, 1986a, b; Patton, 1988; Hansen *et al.*, 1990; Ringdal *et al.*, 1992; Israelsson, 1992; Priestley and Patton, 1997; Schlittenhardt, 2001; Patton and Schlittenhardt, 2005; Zhao *et al.*, 2008, Shin *et al.*, 2010). Zhao *et al.* (2008) used both the third-peak (TP) amplitude and the rms amplitude to measure *Lg* magnitudes for 24 regional events in northeast China and the Korean peninsula and obtained a regional *Lg*-wave magnitude which agrees with the global body-wave magnitude. However, the magnitude measurement is critically dependant on the knowledge of the regional attenuation. Zhao *et al.* (2008) calculated the $m_b(Lg)$ of NKT1 to be 3.93 ± 0.10 based on a constant crustal attenuation model, $Q(f) = 420 \cdot f^{0.15}$, developed by Xie *et al.* (2006), where Q is the quality factor, and f is the frequency. By analyzing *Lg* coda waves, Hong *et al.* (2008) obtained the *Lg* Q_0(1 Hz Q) for the Korean peninsula to be 1025 for pure continental paths and 366 for continental margin paths. Chun and Henderson (2009) obtained another attenuation model, $Q(f) = 317 \cdot f^{0.343}$, based on *Lg*-wave propagation in northernmost North Korea. Later, using the *Lg*-wave data from NKT1, a similar model, $Q(f) = 345 \cdot f^{0.38}$, was obtained for the China–North Korea border by Chun *et al.* (2009). These authors suggested that the difference between the USGS body-wave magnitude $m_b(P) = 4.3$ and the *Lg*-wave magnitude $m_b(Lg) = 3.93$ by Zhao *et al.* (2008) might result from the different attenuation models that were used. Most recently, Zhao *et al.* (2010) developed a broadband tomographic *Lg*-wave attenuation model in and around northeast China. This Q model covers most of the *Lg*-wave paths from the North Korean test site (NKTS) to major regional stations and will be used in this paper for measuring the *Lg*-wave magnitude.

Recently, much effort has been devoted to estimating the yields of the two North Korean nuclear explosions. Herrmann *et al.* (2007) and Koper *et al.* (2008) calculated the seismic moment of NKT1 by using regional *Rg* waves recorded at stations MDJ and INCN and obtained the explosion yield as a function of the source depth and the regional velocity model. Based on the global body-wave magnitude of m_b 4.3 and the full coupled hard-rock magnitude–yield relation by Murphy (1996), Kim and Richards (2007) obtained the yield of NKT1 to be approximately 0.6 kt. Using a regional network located in northeast China and the Korean region, Zhao *et al.* (2008) calculated the *Lg*-wave magnitude for NKT1 as $m_b(Lg) = 3.93$. Then, by adopting the empirical magnitude–yield relation for a fully coupled hard rock condition, they estimated the yield for NKT1 to be 0.48 kt.

In this study, digital broadband seismograms recorded by an extended regional network in northeast China and South Korea are used to investigate the source signature of the second North Korean nuclear test. We first compare regional seismic characteristics between the two North Korean nuclear explosions and then estimate the *Lg*-wave magnitude and yield of NKT2.

Data

Two different data sets are combined and used in this study. The first data set is from seven permanent broadband stations, CN2, SNY, BNX, DL2, XLT, TIA, and HEH, which are affiliated with the China National Digital Seismic Network (CNDSN) operated by the China Earthquake Networks Center (CENC) since December 2000. The second dataset includes recordings from May 1994 to the present from four permanent stations, MDJ, INCN, BJT and HIA, which belong to the Global Seismographic Network (GSN) operated by the USGS and the Incorporated Research Institutions for Seismology consortium (IRIS). Shown in Figure 1 are locations of these digital stations. All stations are located in China except for INCN, which is located in South Korea.

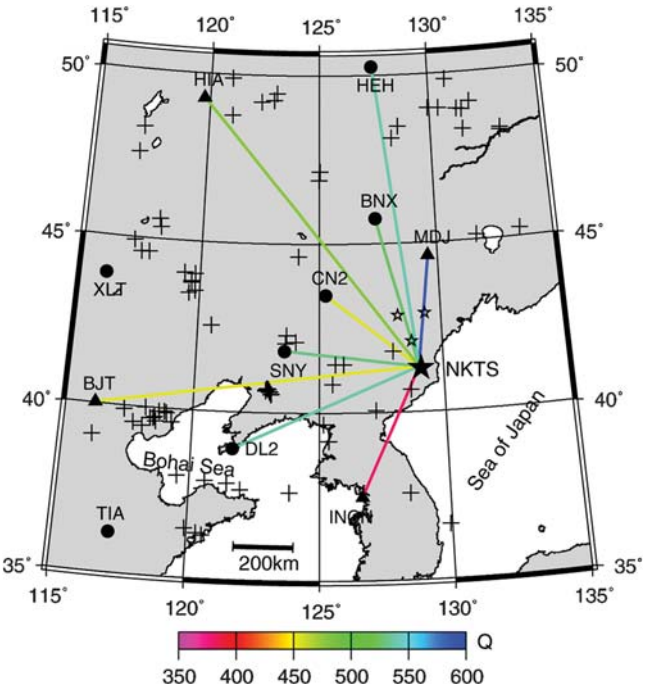

Figure 1. Map showing the locations of the NKTS (solid star), CNDSN (solid circles), and GSN (triangles) stations used in this study. Also illustrated in the figure are epicenters of earthquakes (crosses) that occurred between December 1995 and May 2009 and three small chemical explosions (hollow stars) with known yields. The colors on the great circle ray paths from the NKTS to individual stations denote the average path Q extracted from the *Lg*-wave Q model. Note that the Q values vary between 379 and 589 as listed in Table 3.

Table 1
Station Parameters and Site Corrections for *Lg*-Wave Magnitudes

Station	Latitude (° N)	Longitude (° E)	Elevation (m)	Sampling Rate (s^{-1})	Site Corrections for $m_b(Lg, TP)$ Correction	S.D.	Number	Site Corrections for $m_b(Lg, rms)$ Correction	S.D.	Number	Site Rock	Network
MDJ	44.62	129.59	200	40	0.030	0.249	73	0.030	0.239	73	Granite	GSN
CN2	43.80	125.45	223	50, 100	0.045	0.169	58	0.029	0.163	58	Shale	CNDSN
INCN	37.48	126.63	419	40	−0.109	0.462	63	−0.108	0.457	62	Unknown	GSN
SNY	41.83	123.58	54	50, 100	0.077	0.175	50	0.08	0.169	50	Hybrid granite	CNDSN
BNX	45.74	127.41	198	50, 100	0.009	0.167	51	0.005	0.171	51	Granitic diorite	CNDSN
DL2	38.91	121.63	62	50, 100	−0.06	0.244	44	−0.062	0.238	44	Quartzite	CNDSN
BJT	40.02	116.17	137	20	0.1	0.252	69	0.109	0.242	69	Gravel	GSN
HIA	49.27	119.74	610	20	−0.05	0.188	80	−0.042	0.174	80	Andesite	GSN
XLT	43.89	116.07	1020	50, 100	−0.017	0.185	42	−0.016	0.169	42	Granite	CNDSN
TIA	36.21	117.12	300	50, 100	−0.055	0.25	30	−0.053	0.242	29	Quartz sandstone	CNDSN
HEH	50.25	127.41	168	50, 100	−0.003	0.229	47	−0.016	0.229	47	Granite	CNDSN

The distances from these stations to the NKTS are between 372 and 1152 km, within which various types of regional phases are well developed. Both CNDSN and GSN stations are equipped with broadband instruments that have nearly flat velocity responses between 0.03 and 8.0 Hz, and their sampling rates vary among 20, 40, 50, and 100 per second. The detailed information of these stations is listed in Table 1, where the locations of CNDSN stations are from Shen *et al.* (2008). Eighty-two regional seismic events, including two North Korean nuclear explosions, three small chemical explosions conducted in 1998 for seismic deep sounding purpose, and a group of regional earthquakes, were recorded by this network between December 1995 and May 2009. The location of the NKTS and epicenters of these earthquakes and chemical explosions are indicated in Figure 1 and listed in Ⓔ Table S1 in the electronic supplement to this paper. This data set is used for calibrating the network and investigating the North Korean nuclear explosions.

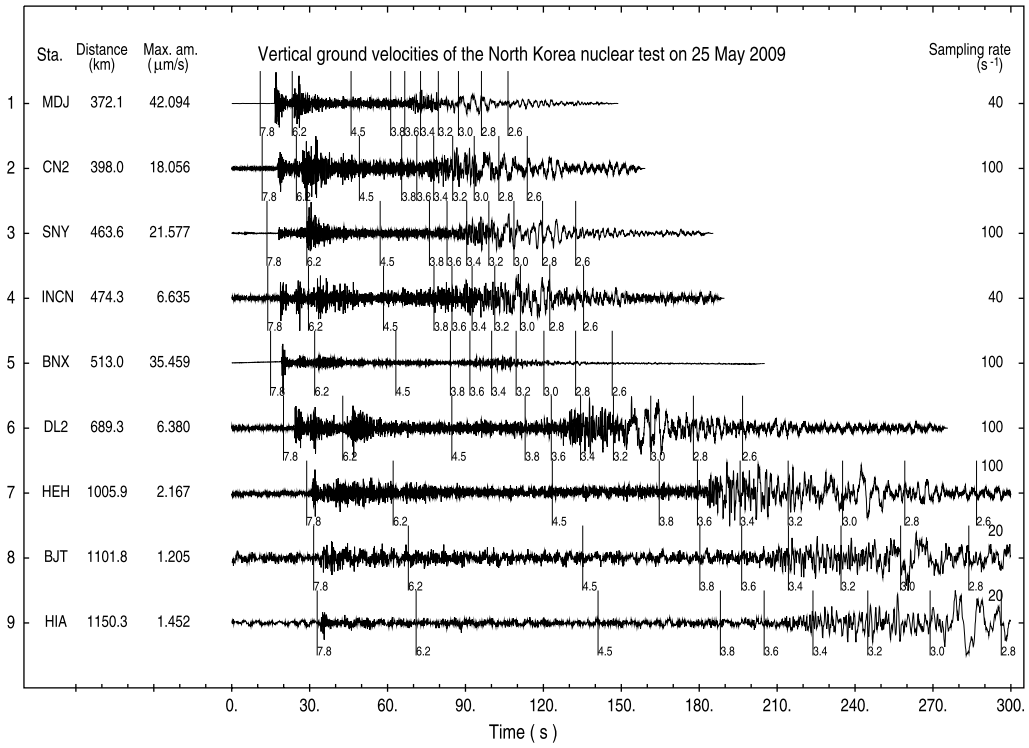

Figure 2. Vertical ground velocities observed from the 25 May 2009 North Korean nuclear explosion. The traces are ordered according to their epicentral distances. The station names and peak amplitudes in μm/s are listed on the left side, and the corresponding sampling rates are listed on the right side. The vertical bars and numbers on the traces indicate apparent group velocities.

Illustrated in Figure 2 are vertical ground velocities from NKT2 with epicentral distances ranging between 372 and 1150 km. On the left are the station codes, epicentral distances, and maximum amplitudes measured in μm/s. The short bars on the seismograms are group velocities. The dataset spans approximately 180 degrees in azimuth and covers almost all possible directions for continental paths (see Fig. 1). The signal-to-noise ratios are excellent. As expected for an explosion source, the seismograms show impulsive *Pn* and *Pg* phases, particularly for stations within 1000 km. Well developed *Lg* waves can be observed at all stations. Because of the shallow source depth, prominent Rayleigh waves can be seen in these seismograms. According to Rapine and Ni (2003), *Sn* waves propagate with low efficiency in northeast China and the Korean peninsula. Considering that an explosion is not an efficient *S*-wave source, its *Sn* phase may be even weaker. Regional seismograms from the North Korean nuclear tests and regional earthquakes do not show clear *Sn* phases (see Fig. 2) although there is still energy appearing in the traditional *Sn*-wave group velocity window. We will not further analyze *Sn* waves in this study.

Comparisons between Waveforms and Spectra from Two Nuclear Tests

We investigate the vertical component waveforms from NKT1 and NKT2. The following group velocity windows are used for measuring different regional phases: *Pn*, 7.8–6.4 km/s; *Pg*, 6.3 − 5.1 km/s; *Lg*, 3.7 − 2.9 km/s; and Rayleigh wave, 5.0 − 2.0 km/s. In order to improve the signal-to-noise ratio, *Pn*, *Pg*, and *Lg* waves are band-pass-filtered from 0.5 or 1.0 Hz to 10 Hz, and the Rayleigh wave is filtered between 8 and 30 s. The epicenters of the two North Korean explosions are separated by only 2.4 km (Wen and Long, 2010). Therefore, regional waves from these two explosions travel to a station on nearly the same path, and their differences should mainly result from near source factors such as yield, depth of burial, and very local 3D overburden structures including topography (Rodgers *et al.*, 2010). Waveform cross-correlation is used to measure the similarities of the waveforms from the two events. Following Salzberg and Marshall (2007), we also calculate integrated envelopes from waveform data and use them to estimate the ratio between the sizes of two nuclear tests. As examples, Figure 3 illustrates some results for *Pn*, *Pg*, *Lg*, and Rayleigh waves at selected stations. In Figure 3, for each station/phase, the upper, middle, and lower panels are vertical component waveforms from the two events, their cross-correlation function, and integrated waveform envelope, respectively.

Being the first arrival in a regional seismogram, the *Pn* wave is less affected by other phases. In addition, the *Pn* wave mainly travels along the uppermost mantle and is relatively insensitive to the layered structure of the crust. *Pn* waves from the two explosions are highly correlated, particularly for their early parts. The cross-correlation function using the first 1 s of *Pn* waveforms is illustrated in the middle panel of Figure 3a, along with the maximum correlation coefficient, γ. The coherency of the *Pn* coda is relatively low compared to the direct *Pn*, likely due to scattering processes. Shown in the lower panel are integrated waveform envelopes for both events, where the solid line is for NKT2, dashed line is for NKT1, and thicker solid line is for NKT1 multiplied by a best fit ratio σ. We see that, apart from a constant, the integrated envelopes are well matched in the first 4–6 s. The ratio σ, which is labeled in the panel, measures the amplitude ratio between the two events.

The regional *Pg* wave is mainly composed of multiply-reflected, postcritical *P* waves trapped in the upper crust (Shurbet, 1960; Langston and Helmberger, 1974; Langston, 1982). Figure 3b compares *Pg* waveforms for station SNY. Compared to the *Pn* waves, the *Pg* phases are less coherent perhaps because there are more scattering processes involved in *Pg* propagation. The cross-correlation is calculated using the first 12 s of *Pg* waves, and the maximum correlation coefficients are low and decrease with increase of the epicentral distance. The integrated energy envelopes are calculated for *Pg* waves, and the curves for the two explosions match well, apart from a scale factor.

The most prominent regional phase is the *Lg* wave, which is a guided wave sampling the crust relatively evenly. It is also sensitive to the characteristics of the free surface and the Moho. Illustrated in Figure 3c are comparisons for *Lg* waves recorded at station DL2. Although the two sources are closely located, their waveform coherence is low, indicating the strong scattering of *Lg* in the crustal waveguide. Their integrated waveform envelopes are well matched, apart from a ratio. Due to their shallow depth, underground explosions often generate more developed Rayleigh waves, compared to earthquakes. We use a zero-phase Butterworth filter between 8 and 30 s to isolate the Rayleigh mode from other high-frequency signals, and the result for station HIA is shown in Figure 3d. Due to its very long wavelength, a Rayleigh wave is insensitive to the detailed near-source structures and the small-scale heterogeneities along the path. The waveforms from the two explosions have very high correlation coefficients. Their integrated waveform envelopes are also plotted for comparison. We also compare the entire regional wave trains from the two explosions. For the entire wave trains, the coherency is low, but the integrated waveform envelopes are very similar. In these analyses, the epicenters of the two events are very close and the observations are made at the same stations. Thus, wave propagation paths should be almost the same, and effects from structures beneath the stations can be ruled out. Table 2 lists the obtained γ and σ for all eight stations. Our results indicate that certain phases from the two events have high similarity. Because long wavelength waves tend to ignore details in sources and near-source structures, the Rayleigh waves are highly correlated and have an average correlation coefficient $\gamma = 0.75$. The early part of the *Pn* waves are also highly correlated and have an average correlation coefficient $\gamma = 0.77$ indicating that *Pn* is not affected by the small differences in crust–upper

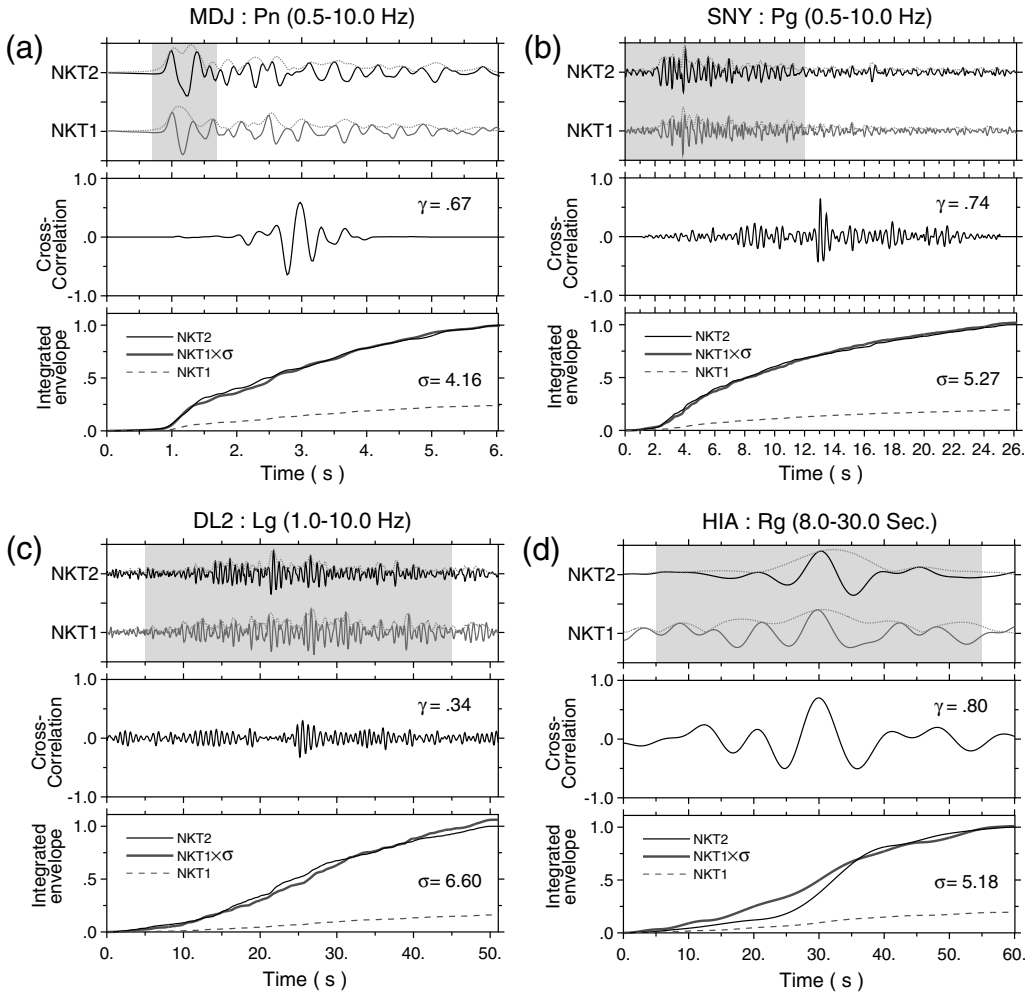

Figure 3. Comparison between regional waveforms from the two North Korean nuclear tests at selected stations. For each station, band-pass-filtered waveforms and their envelops are shown in the upper panel. Shown in the middle panels is the cross-correlation function. Illustrated in the lower panel are integrated amplitude envelopes. Note that the curve from NKT1 has been multiplied by a factor to match that from NKT2. The maximum correlation coefficientsγ and the ratio σ between the integrated envelopes are labeled in the figure.

mantle structures. However, the later part of the *Pn*, i.e., the *Pn* coda, shows reduced similarity (see Fig. 3a). This may be partially due to a scattering effect along the propagation path (Avants *et al.*, 2011) or because different local 3D structures in the two source regions cause different scattering reverberations (Rodgers *et al.*, 2010). For waves such as *Pg* and *Lg*, multiple scattering plays an important role in their propagation. Under this circumstance, their detailed waveforms are

Table 2
Cross-Correlation Coefficients (γ), Ratios of the Integrated Amplitude Envelopes (σ), and Spectral Ratios (κ) between the Two NKTS Explosions

	Pn			*Pg*			*Lg*			Rayleigh Wave		Full Wave	
Station	γ	σ	κ	γ	σ	κ	γ	σ	κ	γ	σ	γ	σ
MDJ	0.67	4.16	3.63	0.58	3.94	4.02	0.34	3.53	3.66	0.88	4.68	0.26	3.88
CN2	0.92	7.23	4.33	0.67	5.43	4.66	0.37	4.59	4.17	0.78	4.28	0.35	5.21
SNY	0.67	4.04	4.13	0.74	5.27	5.65	0.55	4.21	4.58	0.91	4.66	0.31	4.15
BNX	0.67	8.06	6.71	0.53	7.23	6.36	0.4	4.57	4.24	0.48	1.67	0.35	5.33
DL2	0.9	9.17	10.38	0.64	10.29	12.34	0.34	6.6	6.15	0.72	5.71	0.44	9.48
INCN	0.9	3.51	3.77	0.26	3.59	3.73	0.21	2.36	3.27	0.52	2.13	0.44	3
BJT	0.56	5.53	—	0.29	3.94	—	0.33	3.56	3.73	0.91	3.49	0.95	3.66
HIA	0.62	3.86	—	0.36	2.53	—	0.3	3.02	4.62	0.8	5.18	0.97	2.48
Average	0.74	5.7	5.49	0.51	5.28	6.13	0.36	4.06	4.3	0.75	3.98	0.51	4.65
S.D.	0.14	2.18	2.65	0.18	2.48	3.2	0.1	1.28	0.88	0.17	1.44	0.29	2.18

very sensitive to even slightly different waveguide structures resulting in very low correlation coefficients for these waves. For *Pg* waves, average $\gamma = 0.51$, and for *Lg* waves, average $\gamma = 0.36$. On the other hand, the scattering also makes these waves sample the radiation patterns and crust waveguide structures relatively evenly, and their statistical properties, e.g., rms amplitudes and spectra, are relatively stable and can be used for measuring the integral properties of the sources. The integrated waveform envelope is a statistical measurement as well. The ratio σ between the integrated waveform envelopes from the two events should measure the relative size of the two explosions. The ratios for different phases averaged from eight stations are *Pn*, 5.7; *Pg*, 5.28; *Lg*, 4.06; and Rayleigh wave, 3.98 (see Table 2) with the largest value from the *Pn* wave, which has the highest frequency content, and the smallest value from the Rayleigh wave, which has the lowest frequency content. In addition to effects from propagation, the differences in ratios may result from these two events having different sizes, thus different corner frequencies, with each phase sampling different frequency content within the source spectra.

Similarly, we can measure amplitude ratios from wave spectra for the two NKTS explosions. The band passes used for different phases are for *Pn* and *Pg*, 0.5–5.0 Hz; and *Lg*, 0.5–1.5 Hz. Spectral ratios from different phases and stations are listed in Table 2 as κ. These ratios are very close to the results from waveform measurements, and the network average indicates that the spectral amplitudes from NKT2 are approximately five times those from NKT1.

The *Lg*-Wave Magnitude $m_b(Lg)$

Following Zhao *et al.* (2008), we use both the TP amplitude method (Nuttli,1973, 1986a) and the rms-amplitude method (Patton and Schlittenhardt, 2005) to calculate the *Lg*-wave magnitude. The $m_b(Lg)$ can be obtained with

$$m_b(Lg) = 5.0 + \log_{10}[A(\Delta_0)/C]. \quad (1)$$

This equation compares the observed *Lg*-wave amplitude from an unknown magnitude event with the amplitude from a known reference event at a reference distance. In equation (1), the constant C is the *Lg*-wave amplitude caused by an $m_b = 5.0$ event at a reference distance $\Delta_0 = 10$ km, and its value is $C = 110$ μm, for the TP method (Nuttli, 1973, 1986a), and $C = 90$ μm for the rms method (Patton and Schlittenhardt, 2005). The amplitude $A(\Delta_0)$ can be obtained by extrapolating the observed *Lg*-wave amplitude $A(\Delta)$ from the unknown magnitude event using

$$A(\Delta_0) = A(\Delta) \cdot G(\Delta, \Delta_0) \cdot \Gamma(\Delta, \Delta_0, f), \quad (2)$$

where Δ is the epicentral distance and $G(\Delta, \Delta_0)$is the geometrical spreading from Δ to Δ_0. For the TP method (Nuttli, 1973, 1986a)

$$G(\Delta, \Delta_0, TP) = (\Delta/\Delta_0)^{1/3}[\sin(\Delta/111.1)/\sin(\Delta_0/111.1)]^{1/2}, \quad (3)$$

and for the rms-amplitude method (Yang, 2002; Patton and Schlittenhardt, 2005),

$$G(\Delta, \Delta_0, \text{rms}) = (\Delta/\Delta_0)^{1.0}. \quad (4)$$

In equation (2),

$$\Gamma(\Delta, \Delta_0, f) = \exp\left[-\frac{\pi f}{V} \cdot B(\Delta, \Delta_0, f)\right] \quad (5)$$

is the attenuation factor, where f is the frequency, V is the *Lg* group velocity, and

$$B(\Delta, \Delta_0, f) = \int_{\Delta_0}^{\Delta} \frac{ds}{Q(x, y, f)} \quad (6)$$

is the integral of attenuation along the great circle wave path. The *Lg* wave quality factor $Q(x, y, f)$, which is a function of the frequency and surface locations, is crucial in determining *Lg*-wave magnitude. Zhao *et al.* (2010) developed a high-resolution broadband *Lg*-wave attenuation model in and around northeast China using a large regional dataset. With this *Lg* Q model, the *Lg*-wave attenuation along the great circle path can be calculated using equations (5) and (6).

To calculate *Lg*-wave magnitude with equations (1)–(6), we first deconvolve the instrument response from the observed broadband vertical component seismograms and then convolve the seismograms with the WWSSN instrument response to simulate short-period records. A group velocity window between 3.6 and 3.0 km/s is used to pick *Lg* waves. Both TP amplitude and rms amplitude are measured, and the rms amplitude is corrected for the pre-*P* noise (see, e.g., Zhao *et al.*, 2008). Next, we extrapolate the observed amplitude to the reference distance using equations (2)–(4) and the *Lg*-wave attenuation model. The *Lg*-wave group velocity is chosen as 3.5 km/s, and the dominant frequency is calculated by counting the zero crossings. Finally, we use equation (1) to calculate the *Lg*-wave magnitude for both the TP and rms methods.

Before using the regional network to determine the magnitude of NKT2, we calibrate the network using an historical dataset composed of 82 regional events, including a group of earthquakes and two nuclear explosions. The epicenters of these events are illustrated in Figure 1, and their parameters are listed in Ⓔ Table S1, available in the electronic supplement to this paper. We first calculate *Lg* magnitudes $m_b(Lg,$ TP) and $m_b(Lg,$ rms) for 82 events at all stations. The network-averaged magnitudes for individual events are then obtained. Next, the differences between the station magnitudes and the network magnitudes are calculated for individual stations. We then average these differences at individual stations to obtain the station corrections, which are listed in Table 1.

These station corrections are used for removing the effect of local structures beneath the stations. Both $m_b(Lg, \text{TP})$ and $m_b(Lg, \text{rms})$, along with their body-wave magnitudes $m_b(P)$ reported by ISC, NEIC, BJI (Beijing Regional Network) and SKHL (Sakhalin Regional Network) are plotted in Figure 4 to check for any systematic bias. The generally linear relation and the unit slope demonstrate that the *Lg*-wave magnitudes obtained in this region are consistent with the catalog body-wave magnitude.

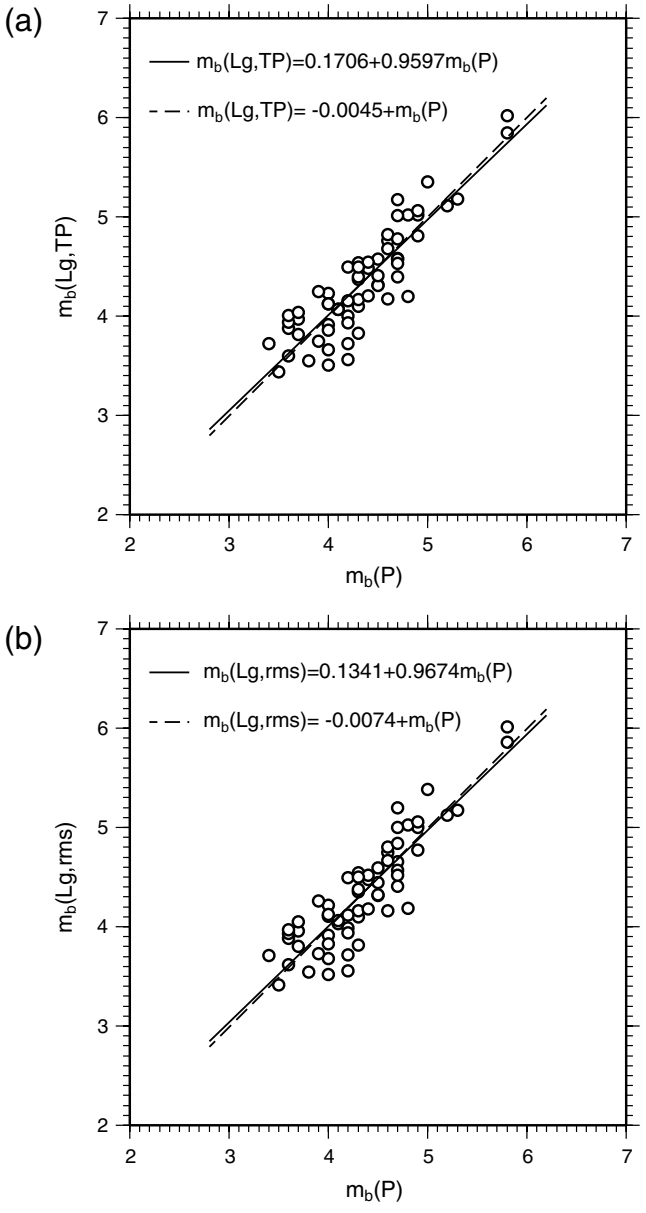

Figure 4. Comparisons between the global body-wave magnitudes and the regional *Lg*-wave magnitudes for all 82 regional events listed in Ⓔ Table S1 (available in the electric supplement to this paper) with (a) $m_b(Lg, \text{TP})$ versus $m_b(P)$ and (b) $m_b(Lg, \text{rms})$ versus $m_b(P)$. The solid lines are from least squares fittings and the dashed lines are for a fixed unit slope.

Finally, we use the calibrated network to obtain the *Lg*-wave magnitude for NKT2. The average *Lg Q* values along different paths are extracted from the attenuation model and illustrated in Figure 1 and Table 3. Note that the path *Q* values vary between 350 and 600, with the continental paths from the NKTS to MDJ, HEH, BNX, HIA, CN2, and SNY are characterized by relatively higher *Q* values, compared to the paths partially crossing the continental margin to INCN, or passing through the very low *Q* Bohai Bay basin (Zhao *et al.*, 2010) to BJT and DL2. Listed in Table 3 are station names, *Lg*-wave amplitudes, and magnitudes from individual stations, along with the network-averaged magnitude $m_b(Lg) = 4.53 \pm 0.12$ for NKT2.

Yield Estimation from the *Lg*-Wave Magnitude

For an uncalibrated test site such as the NKTS, the empirical m_b-yield scaling laws from other calibrated test sites may be transportable for estimating the event yield if proper assumptions on the crustal structures and detonation environment can be made. Several such scaling laws exist. Nuttli (1986a) obtained an $m_b(Lg)$-yield scaling law for the water-saturated site conditions at the Nevada Test Site (NTS),

$$m_b = 3.943 + 1.124 \log Y - 0.0829(\log Y)^2, \qquad (7)$$

where m_b is the *Lg*-wave magnitude and *Y* is the yield in kt. Later this relationship was found to provide reasonably accurate yield estimates for explosions in other areas of the United States and in the French Sahara (Nuttli, 1986a). Instead, Ringdal *et al.* (1992) and Murphy (1996) used another $m_b(P)$-yield relationship for stable regions such as the East Kazakhstan test site,

$$m_b = 4.45 + 0.75 \log Y. \qquad (8)$$

The third one is the modified $m_b(P)$-yield relation for a fully coupled explosion in the Novaya Zemlya region (Bowers *et al.*, 2001),

$$m_b = 4.25 + \beta \cdot \log Y, \qquad (9)$$

where β is 0.75 for $Y \geq 1$ kt and 1.0 for $Y < 1$ kt. The different slopes for different yields are based on the consideration that small explosions are likely to be overburied, and depth of burial might be fixed at 122 m (standard burial depth for a 1 kt explosion). These listed empirical relations are mostly supported by observations with larger explosions. For example, there is no observation of a less than 10-kt explosion to support equation (7) and very little data for explosions below 1 kt to support equations (8) and (9). Shown in Figure 5 are all three m_b-yield relations, where sections supported by data are illustrated using solid lines and the extrapolated parts are illustrated using dashed lines. These relations give similar yield estimates for events between m_b 5 and 7, but are more scattered for smaller events.

Table 3
Magnitude and Yield Estimations

Station	Distance (km)	Sampling Rate (s^{-1})	Measured $A(\Delta)(\mu m)$ TP	Measured $A(\Delta)(\mu m)$ rms	Measured $f(Lg)$ (Hz)	Path Q	$m_b(Lg)$ TP	$m_b(Lg)$ rms	Corrected $m_b(Lg)$ TP	Corrected $m_b(Lg)$ rms	Yield (kt) TP	Yield (kt) rms
MDJ	372.1	40	0.904	0.434	1.276	595	4.526	4.557	4.500	4.534	2.16	2.39
CN2	398.0	100	0.816	0.338	1.190	464	4.592	4.563	4.550	4.541	2.51	2.44
SNY	463.6	100	0.918	0.363	1.168	497	4.725	4.687	4.652	4.614	3.44	3.06
BNX	513	100	0.525	0.208	1.385	525	4.62	4.59	4.615	4.593	3.06	2.86
DL2	689.3	100	0.366	0.141	1.325	537	4.707	4.686	4.771	4.755	4.95	4.71
INCN	474.3	40	0.276	0.121	1.179	381	4.355	4.365	4.469	4.481	1.96	2.03
HEH	1005.9	100	0.145	0.049	0.992	546	4.493	4.444	4.501	4.467	2.16	1.95
BJT	1101.8	20	0.062	0.024	1.045	455	4.427	4.442	4.332	4.341	1.29	1.32
HIA	1150.3	20	0.065	0.025	0.912	478	4.335	4.351	4.389	4.4	1.53	1.58
Network average	685.4	—	0.453	0.189	1.164	498	4.531	4.521	4.531	4.525	2.56	2.48
Standard deviation	315.5	—	0.352	0.156	0.156	62	0.142	0.126	0.135	0.123	1.12	1.01
Network yield†									2.370	2.330		

†Calculated from network average magnitudes.

The body-wave magnitude $m_b(Lg)= 4.53$ obtained for NKT2 is shown in Figure 5 as a horizontal dashed line, which intersects these empirical relations to give the yields of 1.27 kt (Ringdal *et al.*, 1992; Murphy, 1996), 2.35 kt (Bowers *et al.*, 2001), and 3.50 kt (Nuttli, 1986a).

The northeast China–North Korea region is covered by continental crust (Zhang *et al.*, 2002; Li and Yuan, 2003). The region surrounding the NKTS is dominated by three types of rocks including prophyritic biotite granite, fine-grained granite, and diorite (Denny *et al.*, 1996). The crustal *Lg* attenuation tomography reveals that this region has a relatively high and uniform *Lg Q* (Xie *et al.*, 2006; Zhao *et al.*, 2010). This suggests that the NKTS is likely a hard-rock site in an area with stable continental crust.

The *Pn* wave mainly propagates in the uppermost mantle. The *Pn* velocity represents the properties of the material right beneath the Moho, and hence is empirically an indicator of attenuation of a teleseismic *P* wave within the upper mantle (Marshall *et al.*, 1979). We investigate the *Pn* velocity in a region including the NKTS and our station network. Previously published *Pn* speed beneath northeast China and its surrounding region varies widely between 7.4 and 8.0 km/s (Rapine and Ni, 2003; Wang *et al.*, 2003; Hearn *et al.*, 2004; Liang *et al.*, 2004; Pei *et al.*, 2007). On the other hand, with known epicenter locations and relatively accurate source depths, the travel time observations from nuclear explosions provide useful data for accurate *Pn* velocity measurement. Using 15 first arrival data from the two NKTS explosions, the crustal thickness models (Zhu *et al.*, 2006; CRUST 2.0, available at http://igppweb.ucsd.edu/~gabi/crust2.html, last accessed May 2010), the station locations and elevations, and assuming the two explosions are buried at a depth of 1000 m, we estimate the average *Pn* velocity around the northeast China–North Korea region to be 8.0 km/s. This value is lower than the *Pn* velocities in East Kazakhstan (8.3 km/s; Marshall *et al.*, 1979) but higher than those found at NTS (7.6–7.8 km/s; Hearn *et al.*, 1994; Tinker and Wallace, 1997) and is comparable to Novaya Zemlya (8.05 km/s by Ringdal *et al.* 1997).

In August 1998, for the purpose of refraction seismology, a group of chemical explosions with nominal yields between 1.0 and 2.0 tons were detonated in the China–North Korea border area (Zhang *et al.*, 2002) and recorded by GSN stations MDJ, HIA, BJT, and INCN. From the Non-Proliferation Experiment (NPE) it is known that chemical explosions using TNT are more efficient at generating seismic signals by about a factor of 2, compared to a nuclear explosion (Denny *et al.*, 1996). The chemical explosions in the China–North Korea border area used an ammonium nitrate explosive (X. K. Zhang personal comm., 2008). The power of this type of explosive can vary depending on different manufacturers but it is generally less powerful than TNT. Assuming that the power of the ammonium nitrate explosive is roughly 0.5 times that of TNT, and that a TNT explosion is twice as efficient as a nuclear explosion, we estimate that an explosion using an ammonium nitrate explosive has similar efficiency compared to the nuclear explosion. The locations of these chemical explosions are indicated in Figure 1 as open stars, and their source parameters, including locations, nominal yields, and source depths, provided by the Geophysical Exploration Center of the China Earthquake Administration (GECCEA) are listed in Table S1. We calculate their regional magnitudes using the same method for processing the nuclear explosions and earthquakes, and the results are also listed in Table S1. The m_b–yield relations for these small chemical explosions are illustrated as circles in Figure 5. It appears that these chemical explosions favor the fully coupled relations determined by Ringdal *et al.* (1992), Murphy (1996), and Bowers *et al.* (2001) more than the relation established by Nuttli (1986a). These data points are very close to the relation in equation (9), particularly if a slope of 0.75, instead of

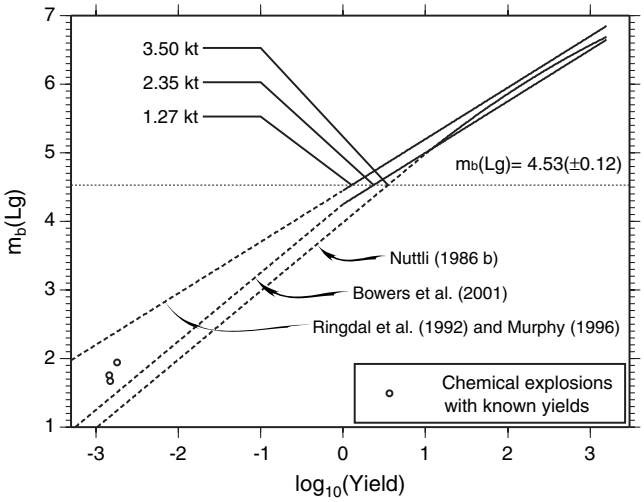

Figure 5. Empirical magnitude–yield relations from Ringdal *et al.* (1992), Murphy (1996), Bowers *et al.* (2001), and Nuttli (1986a), where sections supported by observations are illustrated by solid lines, while the dashed lines are extrapolations. The horizontal dashed line indicates the estimated $m_b(Lg)= 4.53$ for NKT2. Also illustrated in this figure are magnitude–yield relations for three chemical explosions with known yields (circles).

1.0, is used for the yield below 1 kt. This can be explained by the fact that these chemical explosions were detonated at very shallow depths and did not follow a minimum burial depth. Observations from these small chemical explosions provide a constraint at the low yield end.

Considering the regional geology, the *Pn* velocity, and the calibrated small chemical explosions, we prefer the fully coupled hard-rock site equation (9) by Bowers *et al.* (2001) for estimating the yield of the 25 May 2009 North Korean nuclear explosion. Based on this relation, the yields for NKT2 calculated from the network-averaged $m_b(Lg, \text{TP})$ and $m_b(Lg, \text{rms})$ are 2.37 and 2.33 kt, respectively. We take their average, 2.35 kt, as our preferred estimate and list it in Table 3.

Discussions and Conclusion

Based on a regional seismic network composed of 11 broadband stations in northeast China and South Korea, we investigate the explosive yield of the 25 May 2009 North Korean nuclear test. The stations range between 372 and 1152 km from the NKTS. Regional data from the two nuclear tests, three chemical explosions, and a group of regional earthquakes were recorded between December 1995 and May 2009. We compare the regional phase characteristics between the two nuclear explosions. Both the integrated waveform envelops and the spectral amplitudes suggest that the amplitudes of seismic records from the NKT2 are approximately five times those from the NKT1. To accurately calculate the *Lg*-wave magnitude for nuclear explosions, we first use all recorded events to calibrate the regional network. Both $m_b(Lg, \text{TP})$ and $m_b(Lg, \text{rms})$ are calculated, and station corrections are determined. By comparing the corrected *Lg*-wave magnitudes with the global body-wave magnitudes reported from the NEIC, ISC, BJI, and SKHL, both the TP method and the rms method generate consistent results with the global magnitude m_b. The calibrated network is then used to calculate *Lg*-wave magnitudes of the two North Korean nuclear explosions. For NKT1, the *Lg*-wave magnitude is $m_b(Lg)= 3.93$, which is consistent with the previous estimate by Zhao *et al.* (2008), and for NKT2 the *Lg*-wave magnitude is $m_b(Lg)= 4.53$.

The northeast China–North Korea region is mainly covered by continental crust (Zhang *et al.*, 2002; Li and Yuan 2003). The path *Lg Q*s from the NKTS to different stations are between 379 and 589, as shown in Figure 1 and Table 3. Through these paths, *Lg* waves generally propagate in high-*Q* crustal waveguide except for the path to INCN, where it partially crosses the Sea of Japan, and for the paths to BJT and DL2, where the paths partially cross the low *Q* Bohai Bay basin (Zhao *et al.*, 2010). The *Pn* velocity in the northeast China–North Korea region is close to 8.0 km/s, which is similar to the *Pn* velocities in Novaya Zemlya. The surface geology indicates that the region surrounding the NKTS is mainly composed of hard rocks. All of these mentioned factors suggest that the NKTS is likely a hard-rock site in an area with stable continental crust. Therefore, we use the empirical magnitude–yield relation for the fully coupled hard-rock site by Bowers *et al.* (2001) to estimate the yield of the NKT2. With this empirical relation, the yield for NKT2 is 2.35 kt, about 4.9 times the yield of NKT1.

Even with the previously mentioned considerations and assumptions, the yield estimation in an uncalibrated region still involves large uncertainties. Most of these previously obtained empirical relations are from large magnitude events. Applying them to small explosions such as those at the NKTS involves extrapolation over large magnitude and yield ranges. Among those empirical relations, equation (7) directly links the $m_b(Lg)$ with the yield, but the other two equations are between $m_b(P)$ and yield. Although we calibrate the $m_b(Lg)$ with the $m_b(P)$ using earthquake data, bias may still exist for explosions detonated at much shallower depths. Another issue is that these empirical relations are mostly from standard buried explosions, while there is evidence that the two North Korean explosions are overburied. There are trade-offs between estimated yield and the depth of burial. It is commonly accepted that, given an observed m_b, the estimated yield will generally increase with increasing source depth, at least for small magnitude events (e.g., Mueller and Murphy, 1971; Burdick *et al.*, 1984; Denny and Johnson, 1991). Thus, the depth variation is a big source of uncertainty in yield estimation (Bowers *et al.*, 2001; Herrmann *et al.*, 2007; Bonner *et al.*, 2008; Koper *et al.*, 2008).

Many efforts have been made toward simultaneously constraining the yield and the burial depth for the NKTS. Ni *et al.* (2010) emphasized the uncertainties in yield estimation from both empirical relation transportation and burial

depth. They obtained a yield estimate of 1.5 kt at depth 300 m and 2 kt at depth 600 m for NKT1 based on different attenuation models. Similarly, they obtained a preliminary yield estimate of 8 kt at depth 400 m for NKT2. Murphy *et al.* (2010) calculated the network-averaged *Pn* spectral ratios between 1 and 15 Hz. They then compared these ratios with the theoretical Mueller–Murphy source spectral model and estimated the yield for NKT1 as 0.9 kt, if detonated at a depth of 200 m, and 4.6 kt for NKT2, if detonated at a depth of 550 m. They also analyzed teleseismic *P* data and, by assuming a source depth of 200 m, estimated the yield for NKT2 varying between 2.7 and 5.3 kt, depending on the attenuation model. However, they indicated that the observed teleseismic spectral data do not have the resolving power to distinguish between the alternate hypotheses of a 2.7 kt explosion at a depth of 200 m and a 4.8 kt explosion at a depth of 800 m.

The $m_b(P)$ based methods are well described by the theory, while the $m_b(Lg)$ based method has an additional difficulty because *Lg*-wave excitation mechanism is not fully understood. H. Patton (personal comm., 2011) investigated the yield versus depth of burial trade-off curves from $m_b(P)$ and moment magnitude and proposed a method to account for possible m_b bias and the effects of source medium elastic properties on the trade-off curve for the NKTS. By further combining the results from the hydrodynamic simulation and near-field observations, Rougier *et al.* (2011) obtained the minimum yield and depth of burial for the NKT2 as 5.7 kt and 375 m. Based on these newly developed trade-off curves, our measurement on the yield of the NKT2 should be a lower bound and the yield could be larger if the North Korean explosions are extensively overburied.

Data and Resources

Waveforms recorded at the CNDSN stations were collected from the CENC. The data recorded by GSN stations were from the IRIS Data Management Center (DMC) at www.iris.edu (last accessed April 2010). The source parameters of three chemical explosions were provided by GEC-CEA. Some figures were made using the Generic Mapping Tools version 4.3.1 available at www.soest.hawaii.edu/gmt (last accessed April 2010).

Acknowledgments

Howard Patton provided valuable review comments. We thank H. Patton and another anonymous reviewer for their comments, which greatly improved the manuscript. We wish to thank Thorne Lay for many discussions and comments. This research is supported by the National Natural Science Foundation of China (Grant Numbers 41174048, 40974029, and 90714012). Xiao-Bi Xie wishes to thank the Air Force Research Laboratory for support under Contract No. FA9453-11-C-0234.

References

Avants, M., T. Lay, X. B. Xie, and X. N. Yang (2011). Effects of 2D random velocity heterogeneities in the mantle lid and Moho topography on *Pn* geometric spreading, *Bull. Seismol. Soc. Am.* **101,** no. 1, 126–140, doi 10.1785/0120100113.

Bonner, J., R. B. Herrmann, D. Harkrider, and M. Pasyanos (2008). The surface wave magnitude for the 9 October 2006 North Korean nuclear explosion, *Bull. Seismol. Soc. Am.* **98,** 2498–2506, doi 10.1785/0120080929.

Bowers, D., P. D. Marshall, and A. Douglas (2001). The level of deterrence provided by data from the SPITS seismometer array to possible violations of the comprehensive test ban in the Novaya Zemlya region, *Geophys. J. Int.* **146,** 425–438, doi 10.1046/j.1365-246x.2001.01462.x.

Burdick, L. J., T. Wallace, and T. Lay (1984). Modeling near-field and teleseismic observations from the Amchitka test site, *J. Geophys. Res.* **89,** no. B6 4373–4388, doi 10.1029/JB089iB06p04373.

Chun, K.-Y., and G. A. Henderson (2009). *Lg* attenuation near the North Korean border with China, Part II: Model development from the 2006 nuclear explosion in North Korea, *Bull. Seismol. Soc. Am.* **99,** 3030–3038, doi 10.1785/0120080341.

Chun, K.-Y., Y. Wu, and G. A. Henderson (2009). *Lg* attenuation near the North Korean border with China, Part I: Model development from regional earthquake sources, *Bull. Seismol. Soc. Am.* **99,** 3021–3029, doi 10.1785/0120080316.

Denny, M. D., and L. R. Johnson (1991). The explosion seismic source function: Model and scaling laws revisited, in *Explosion Source Phenomenology* S. R. Taylor, H. J. Patton, and P. G. Richards (Editors), American Geophysical Monograph **65,** 1–24, doi 10.1029/GM065p0001.

Denny, M., P. Goldstein, K. Mayeda, and W. Walter (1996). Seismic results from DOE's non-proliferation experiment: A comparison of chemical and nuclear explosions, in *Monitoring a Comprehensive Test Ban Treaty*, E. S. Husebye and A. M. Dainty (Editors), Kluwer Academic Publishers, Dordrecht, 355–364.

Hansen, R. A., F. Ringdal, and P. G. Richards (1990). The stability of rms *Lg* measurements and their potential for accurate estimation of the yields of Soviet underground nuclear explosions, *Bull. Seismol. Soc. Am.* **80,** 2106–2126.

Hearn, T. M., A. C. Rosca, and M. C. Fehler (1994). *Pn* tomography beneath the southern Great Basin, *Geophys. Res. Lett.* **21,** no. 20, 2187–2190, 10.1029/94GL02054.

Hearn, T. M., S. Wang, J. F. Ni, Z. Xu, Y. Yu, and X. Zhang (2004). Uppermost mantle velocities beneath China and surrounding regions, *J. Geophys. Res.* **102,** no. B11301, 11, doi 10.1029/2003JB002874.

Herrmann, R. B., W. R. Walter, and M. E. Pasyanos (2007). Seismic source and path calibration in the Korean peninsula, Yellow Sea and Northeast China, *29th Monitoring Research Review: Ground-Based Nuclear Explosion Monitoring Technologies*, 592–601.

Hong, T. K., and J. Rhie (2009). Regional source scaling of the 9 October 2006 underground nuclear explosion in North Korea, *Bull. Seismol. Soc. Am.* **99,** 2523–2540, doi 10.1785/0120080007.

Hong, T.-K., C.-E. Baag, H. Choi, and D.-H. Sheen (2008). Regional seismic observations of the 9 October 2006 underground nuclear explosion in North Korea and the influence of crustal structure on regional phases, *J. Geophys. Res.* **113,** no. B03305, 15, doi 10.1029/2007JB004950.

Israelsson, H. (1992). RMS *Lg* as a yield estimator in Eurasia, Final Technical Report, PL-TR-92-2117(I), Phillips Laboratory, Hanscom Air Force Base, Massachusetts.

Kim, W.-Y., and P. G. Richards (2007). North Korean nuclear test: Seismic discrimination at low yield, *Eos Trans. AGU* **88,** 158, doi 10.1029/2007EO140002.

Kim, T. S., I.-B. Kang, and G.-Y. Kim (2009). Yield ratio estimates using regional *Pn* and *Pg* from North Korea's underground nuclear explosions, *Geophys. Res. Lett.* **36,** L22302, doi 10.1029/2009GL040495.

Koper, K. D., R. B. Herrmann, and H. M. Benz (2008). Overview of open seismic data from the North Korea event of 9 October 2006, *Seismol. Res. Lett.* **79,** 178–185, doi 10.1785/gssrl.79.2.178.

Kvaerna, T., F. Ringdal, and U. Baadshaug (2007). North Korea's nuclear test: The capability for seismic monitoring of the North Korean test site, *Seismol. Res. Lett.* **78,** 487–497, doi 10.1785/gssrl.78.5.487.

Langston, C. A. (1982). Aspects of *Pn* and *Pg* propagation at regional distances, *Bull. Seismol. Soc. Am.* **72,** 457–471.

Langston, C. A., and D. V. Helmberger (1974). Interpretation of body and Rayleigh waves from NTS to Tucson, *Bull. Seismol. Soc. Am.* **64,** 1919–1929.

Li, X., and X. Yuan (2003). Receiver functions in northeast China—implications for slab penetration into the lower mantle in northwest Pacific subduction zone, *Earth Planet. Sci. Lett.* **216,** 679–691, doi 10.1016/S0012-821X(03)00555-7.

Liang, C. T., X. Song, and J. L. Huang (2004). Tomographic inversion of *Pn* travel times in China, *J. Geophys. Res.* **109,** no. B11304, 19, doi 10.1029/2003JB002789.

Marshall, P. D., D. L. Springer, and H. C. Rodean (1979). Magnitude corrections for attenuation in the upper mantle, *Geophys. J. Roy. Astron. Soc.* **57,** 609–638, doi 10.1111/j.1365-246X.1979.tb06781.x.

Mueller, R., and J. Murphy (1971). Seismic characteristics of underground nuclear detonations Part I. Seismic spectrum scaling, *Bull. Seismol. Soc. Am.* **61,** 1675–1692.

Murphy, J. R. (1996). Type of seismic events and their source descriptions, in *Monitoring a Comprehensive Test Ban Treaty*, E. S. Husebye and A. M. Dainty (Editors), Kluwer Academic Publishers, Dordrecht, 225–245.

Murphy, J. R., B. C. Kohl, J. L. Stevens, T. J. Bennett, and H. G. Israelsson (2010). Exploitation of the IMS and other data for a comprehensive, advanced analysis of the North Korean nuclear tests, in *Proc. of the 2010 Monitoring Research Review: Ground-Based Nuclear Explosion Monitoring Technologies*,M. A Wetovsky and E. F. Patterson (Editors), Orlando, Florida, 21–23 September 2010, 456–465.

Ni, S., D. Helmberger, and A. Pitarka (2010). Rapid source estimation from global calibrated paths, *Seismol. Res. Lett.* **81,** 498–504, doi 10.1785/gssrl.81.3.498.

Nuttli, O. W. (1973). Seismic wave attenuation and magnitude relations for eastern North America, *J. Geophys. Res.* **78,** 876–885, doi 10.1029/JB078i005p00876.

Nuttli, O. W. (1986a). Yield estimates of Nevada test site explosions obtained from seismic *Lg* waves, *J. Geophys. Res.* **91,** 2137–2151, doi 10.1029/JB091iB02p02137.

Nuttli, O. W. (1986b). *Lg* magnitudes of selected East Kazakhstan underground explosions, *Bull. Seismol. Soc. Am.* **76,** 1241–1251.

Patton, H. J. (1988). Application of Nuttli's method to estimate yield of Nevada test site explosions recorded on Lawrence Livermore National Laboratory's digital seismic system, *Bull. Seismol. Soc. Am.* **78,** 1759–1772.

Patton, H. J., and J. Schlittenhardt (2005). A transportable $m_b(Lg)$ scale for central Europe and implications for low-magnitude M_s–$m_b$discrimination, *Geophys. J. Int.* **163,** 126–140, doi 10.1111/j.1365-246X.2005.02663.x.

Patton, H. J., and S. R. Taylor (2008). Effects of induced tensile failure on m_b—M_s discrimination: Contrasts between historic nuclear explosions and the North Korean test of 9 October 2006, *Geophys. Res. Lett.* **35,** L14301, doi 10.1029/2008GL034211.

Pei, S. P., J. M. Zhao, Y. S. Sun, Z. H. Xu, S. Y. Wang, H. B. Liu, C. A. Rowe, M. N. Toksöz, and X. Gao (2007). Upper mantle seismic velocities and anisotropy in China determined through *Pn* and *Sn* tomography, *J. Geophys. Res.* **112,** no. B05312, 16, doi 10.1029/2006JB004409.

Phillips, W. S., H. E. Hartse, and L. K. Steck (2001). Precise relative location of 25-ton chemical explosions using IMS stations, *Pure Appl. Geophys.* **158,** 173–192, doi 10.1007/PL00001154.

Poupinet, G., W. L. Ellsworth, and J. Frechet (1984). Monitoring velocity variations in the crust using earthquake doublets: An application to the Calaveras fault, California, *J. Geophys. Res.* **89,** no. B7 5719–5731, doi 10.1029/JB089iB07p05719.

Priestley, K. F., and H. J. Patton (1997). Calibration of $m_b(Pn)$, $m_b(Lg)$ scales and transportability of the M_o : m_b discriminant to new tectonic regions, *Bull. Seismol. Soc. Am.* **87,** 1083–1099.

Rapine, R. R., and J. F. Ni (2003). Propagation characteristics of *Sn* and *Lg* in northeastern China and Mongolia, *Bull. Seismol. Soc. Am.* **93,** 939–945, doi 10.1785/0120010157.

Ringdal, F., E. O. Kremenetskaya, V. E. Asming, and Y. Filatov (1997). Study of seismic travel-time models for the Barents region, *Semiannual Technical Summary 1 October 1996–31 March 1997, NORSAR Sci. Rept. 2-96/97.*

Ringdal, F., P. D. Marshall, and R. W. Alewine (1992). Seismic yield determination of Soviet underground explosions at the Shagan River test site, *Geophys. J. Int.* **109,** 65–77, doi 10.1111/j.1365-246X.1992.tb00079.x.

Rodgers, A. J., N. A. Petersson, and B. Sjogreen (2010). Simulation of topographic effects on seismic waves from shallow explosions near the North Korean nuclear test site with emphasis on shear wave generation, *J. Geophys. Res.* **115,** no B11309, 27, doi 10.1029/2010JB007707.

Rougier, E., H. J. Patton, E. E. Knight, and C. R. Bradley (2011). Constraints on burial depth and yield of the 25 May 2009 North Korean test from hydrodynamic simulations in a granite medium, *Geophys. Res. Lett.* **38,** L16316, doi 10.1029/2011GL048269.

Salzberg, D., and M. Marshall (2007). Seismic source locations and parameters for sparse networks by matching observed seismograms to semi-empirical synthetic seismograms: Applications to Lop Nor and North Korea, *29th Monitoring Research Review: Ground-based nuclear explosion monitoring technologies* **47,** 2–481.

Schaff, D. P., and P. G. Richards (2004). Repeating seismic events in China, *Science* **303,** 1176–1178, doi 10.1126/science.1093422.

Schimmel, M. (1999). Phase cross-correlations: Design, comparisons, and applications, *Bull Seismol. Soc. Am.* **89,** 1366–1378.

Schlittenhardt, J. (2001). Teleseismic *Lg* of Semipalatinsk and Novaya Zemlya nuclear explosions recorded at the GRF (Gräfenberg) array: Comparison with regional *Lg* (BRV) and their potential for accurate yield estimation, *Pure Appl. Geophys.* **158,** 2253–2274, doi 10.1007/PL00001148.

Schlittenhardt, J., M. Canty, and I. Grunberg (2010). Satellite Earth observations support CTBT monitoring: A case study of the nuclear test in North Korea of Oct. 9, 2006 and comparison with seismic results, *Pure Appl Geophys.* **167,** no. 4–5 601–618, doi 10.1007/s00024-009-0036-x.

Shearer, P. M. (1997). Improving local earthquake locations using the L1 norm and waveform cross correlation: Application to the Whittier Narrows, California, aftershock sequence, *J. Geophys. Res.* **102,** no. B4 8269–8283, doi 10.1029/96JB03228.

Shearer, P. M., J. L. Hardebeck, L. Astiz, and K. B. Richards-Dinger (2003). Analysis of similar event clusters in aftershocks of the 1994 Northridge, California, earthquake, *J. Geophys. Res.* **108,** 14, doi 10.1029/2001JB000685.

Shen, X., H. Zhou, and H. Kawakatsu (2008). Mapping the upper mantle discontinuities beneath China with teleseismic receiver functions, *Earth Planets Space* **60,** 713–719.

Shin, J. S., D.-H. Sheen, and G. Kim (2010). Regional observations of the second North Korean nuclear test on 2009 May 25, *Geophys. J. Int.* **180,** 243–250, doi 10.1111/j.1365-246X.2009.04422.x.

Shurbet, D. H. (1960). The *P* phase transmitted by crustal rock to intermediate distances, *J. Geophys. Res.* **65,** 1809–1814, doi 10.1029/JZ065i006p01809.

Tibuleac, I. M., D. H. von Seggern, J. G. Anderson, K. W. Smith, A. Aburto, and T. Rennie (2008). Location and magnitude estimation of the 9 October 2006 Korean nuclear explosion using the southern Great Basin digital seismic network as a large-aperture array, *Bull. Seismol. Soc. Am.* **98,** 756–767, doi 10.1785/0120070046.

Tinker, M. A., and T. C. Wallace (1997). Regional phase development of the non-proliferation experiment within the western United States, *Bull. Seismol. Soc. Am.* **87,** no. 2, 383–395.

Wang, S., Z. Xu, and S. Pei (2003). Velocity structure of uppermost mantle beneath North China from *Pn* tomography and its implications, *Sci. China Earth Sci.* **46,** 130–140, doi 10.1007/BF02879791.

Waldhauser, F., D. Schaff, P. G. Richards, and W. Y. Kim (2004). Lop Nor revisited: Underground nuclear explosion locations, 1976–1996, from double-difference analysis of regional and teleseismic data, *Bull Seismol. Soc. Am.* **94,** 1879–1889, doi 10.1785/012003184.

Wen, L., and H. Long (2010). High-precision Location of North Korea's 2009 Nuclear Test, *Seismol. Res. Lett.* **81,** 26–29, doi 10.1785/gssrl.81.1.26.

Xie, J., Z. Wu, R. Liu, D. Schaff, Y. Liu, and J. Liang (2006). Tomographic regionalization of crustal *Lg Q* in eastern Eurasia, *Geophys. Res. Lett.* **33,** L03315, doi 10.1029/2005GL024410.

Yang, X. (2002). A numerical investigation of *Lg* geometrical spreading, *Bull. Seismol. Soc. Am.* **92,** 3067–3079, doi 10.1785/0120020046.

Zhang, C. K., X. K. Zhang, J. R. Zhao, B. F. Liu, J. S. Zhang, Z. X. Yang, Y. Hai, and G. W. Sun (2002). Crust-mantle structure of the Changbaishan Tianchi volcanic region and its vicinity: An exploratory study and inferences, *Chinese J. Geophys.* **45,** 862–871.

Zhao, L. F., X. B. Xie, W. M. Wang, and Z. X. Yao (2008). Regional seismic characteristics of the 9 October 2006 North Korean nuclear test, *Bull. Seismol. Soc. Am.* **98,** 2571–2589, doi 10.1785/0120080128.

Zhao, L. F., X. B. Xie, W. M. Wang, J. H. Zhang, and Z. X. Yao (2010). Seismic *Lg*-wave *Q* tomography in and around Northeast China, *J. Geophys. Res.* **115,** no. B08307, 22, doi 10.1029/2009JB007157.

Zhu, J. S., X. L. Cai, J. M. Cao, and Z. Q. Yan (2006). Lithospheric structure and geodynamics in China and its adjacent areas (in Chinese with English abstract), *Geology in China* **33,** 793–803.

Key Laboratory of the Earth's Deep Interior
Institute of Geology and Geophysics
Chinese Academy of Sciences
19 Beituchengxilu Road, Chaoyang District
Beijing 100029, China
zhaolf@mail.igcas.ac.cn
(L.-F.Z., Z.-X.Y.)

Institute of Geophysics and Planetary Physics
University of California at Santa Cruz
1156 High Street
Santa Cruz, California 95064
xxie@ucsc.edu
(X.-B.X.)

Key Laboratory of Continental Collision and Plateau Uplift
Institute of Tibetan Plateau Research
Chinese Academy of Sciences
18 Shuangqinglu Road, Haidian District
Beijing 100085, China
wangwm@itpcas.ac.cn
(W.-M.W.)

Manuscript received 25 May 2011